2003-01-01

Solution of the Navier-Stokes Equations for Transonic Propeller Flows

Fergal Boyle
Technological University Dublin, fergal.boyle@tudublin.ie

Funder: DIT

21st AIAA Applied Aerodynamics Conference
Orlando, Florida
23-26 June, 2003

AIAA-2003-4083

EFFICIENT SOLUTION OF THE NAVIER-STOKES EQUATIONS FOR TRANSONIC PROPELLER FLOWS

Fergal Boyle*
Department of Mechanical Engineering
Dublin Institute of Technology, Bolton St, Dublin 1, Ireland

ABSTRACT

The three-dimensional, compressible, viscous flow field around a general propeller geometry with the inflow at zero angles of incidence and yaw is computed using a Reynolds-Averaged Navier-Stokes equations solver. Results from validation test cases in which the laminar and turbulent incompressible flow over a flat plate are calculated demonstrate the flow solver is capable of accurately capturing boundary-layer behaviour. Euler solutions from flow field calculations around two very different propeller geometries show a high level of accuracy and efficiency. Preliminary results from a viscous flow field calculation around a two-bladed propeller are very encouraging.

INTRODUCTION

The possible fuel savings that can be achieved by an advanced propeller over an equivalent technology turbofan engine operating at competitive speeds and altitudes have been well documented. To-date, however, potential cabin noise problems, the reduction of aviation fuel costs, and the perceived prejudice of the general public towards propeller driven aircraft, have hindered the introduction of advanced propellers on large commercial aircraft.

Meanwhile, propellers with advanced-propeller characteristics have been introduced on regional and general aviation aircraft that were traditionally propeller driven. Currently, interest still remains in the advanced propeller concept both for commercial and military use, as fuel efficiency is of crucial importance in the development of propulsion systems

In order to further improve the aerodynamic and acoustic performance of the advanced propeller, it is necessary to fully understand the complex flow patterns occurring on the blade and hub surfaces and in the general surrounding flow field. To this end, a flow solver has recently been developed to predict the three-dimensional, compressible, viscous flow field around general propeller configurations with the inflow along the main axis of the propeller.

*Lecturer, Member AIAA

The solver, named NAVPROP, solves the Reynolds-Averaged Navier-Stokes equations formulated in a steadily-rotating, blade-attached, non-inertial reference frame. With this formulation the flow can then be treated as steady relative to the propeller. To solve the governing equations, a cell-centre finite-volume scheme is employed. Explicit, multistage, Runge-Kutta time stepping marches the solution towards a steady-state, while local time-stepping, implicit residual averaging, and multigrid are employed to increase the rate of convergence. The computational domain is discretised into a contiguous set of hexahedral cells as part of a C-H grid system.

The development of NAVPROP has been the focus of this work and is described in detail. Results are presented from five test cases completed.

FLOW SOLVER

Governing Equations

The governing equations of viscous flow, i.e., the Navier-Stokes equations, are initially formulated using the flow model of a fixed finite control volume in a non-inertial reference frame that is attached to the rotating propeller[1]. A right-handed Cartesian coordinate system is employed and it is assumed that the propeller rotates with constant angular velocity ω around the x axis. The equations thus obtained are then re-written in partial differential equation form, non-dimensionalised using a standard non-dimensionalisation procedure, and finally transformed to a body-fitted curvilinear coordinate system. Letting ρ, u, v, w, p, and E denote density, the x, y, and z components of the absolute velocity vector, static pressure and total energy per unit volume respectively, the final form of the governing equations in vector form is as follows

$$\frac{\partial (J^{-1}Q)}{\partial t}+\frac{\partial F}{\partial \xi}+\frac{\partial G}{\partial \eta}+\frac{\partial H}{\partial \zeta}=I+\frac{\partial F_v}{\partial \xi}+\frac{\partial G_v}{\partial \eta}+\frac{\partial H_v}{\partial \zeta} \qquad (1)$$

where the vectors are

$$Q=\begin{bmatrix}\rho\\ \rho u\\ \rho v\\ \rho w\\ E\end{bmatrix}$$

$$F = J^{-1}\begin{bmatrix} \rho U \\ \rho u U + \xi_x p \\ \rho v U + \xi_y p \\ \rho w U + \xi_z p \\ (E+p)U - \xi_t p \end{bmatrix}$$

$$G = J^{-1}\begin{bmatrix} \rho V \\ \rho u V + \eta_x p \\ \rho v V + \eta_y p \\ \rho w V + \eta_z p \\ (E+p)V - \eta_t p \end{bmatrix}$$

$$H = J^{-1}\begin{bmatrix} \rho W \\ \rho u W + \zeta_x p \\ \rho v W + \zeta_y p \\ \rho w W + \zeta_z p \\ (E+p)W - \zeta_t p \end{bmatrix}$$

$$I = J^{-1}\begin{bmatrix} 0 \\ 0 \\ \rho\omega w \\ -\rho\omega v \\ 0 \end{bmatrix} \qquad (2)$$

$$F_v = \frac{\sqrt{\gamma} Ma_\infty J^{-1}}{Re_\infty}\begin{bmatrix} 0 \\ \xi_x\tau_{xx} + \xi_y\tau_{yx} + \xi_z\tau_{zx} \\ \xi_x\tau_{xy} + \xi_y\tau_{yy} + \xi_z\tau_{zy} \\ \xi_x\tau_{xz} + \xi_y\tau_{yz} + \xi_z\tau_{zz} \\ \xi_x b_x + \xi_y b_y + \xi_z b_z \end{bmatrix}$$

$$G_v = \frac{\sqrt{\gamma} Ma_\infty J^{-1}}{Re_\infty}\begin{bmatrix} 0 \\ \eta_x\tau_{xx} + \eta_y\tau_{yx} + \eta_z\tau_{zx} \\ \eta_x\tau_{xy} + \eta_y\tau_{yy} + \eta_z\tau_{zy} \\ \eta_x\tau_{xz} + \eta_y\tau_{yz} + \eta_z\tau_{zz} \\ \eta_x b_x + \eta_y b_y + \eta_z b_z \end{bmatrix}$$

$$H_v = \frac{\sqrt{\gamma} Ma_\infty J^{-1}}{Re_\infty}\begin{bmatrix} 0 \\ \zeta_x\tau_{xx} + \zeta_y\tau_{yx} + \zeta_z\tau_{zx} \\ \zeta_x\tau_{xy} + \zeta_y\tau_{yy} + \zeta_z\tau_{zy} \\ \zeta_x\tau_{xz} + \zeta_y\tau_{yz} + \zeta_z\tau_{zz} \\ \zeta_x b_x + \zeta_y b_y + \zeta_z b_z \end{bmatrix}$$

U, V, and W are the contravariant velocity components in the ξ, η, and ζ directions respectively, and are defined as

$$\begin{aligned} U &= \xi_x u + \xi_y v + \xi_z w + \xi_t \\ V &= \eta_x u + \eta_y v + \eta_z w + \eta_t \\ W &= \zeta_x u + \zeta_y v + \zeta_z w + \zeta_t \end{aligned} \qquad (3)$$

and the shear stress terns are

$$\begin{aligned} \tau_{xx} &= \frac{2\mu}{3}\left(2\frac{\partial u}{\partial x} - \frac{\partial v}{\partial y} - \frac{\partial w}{\partial z}\right) \\ \tau_{yy} &= \frac{2\mu}{3}\left(2\frac{\partial v}{\partial y} - \frac{\partial u}{\partial x} - \frac{\partial w}{\partial z}\right) \\ \tau_{zz} &= \frac{2\mu}{3}\left(2\frac{\partial w}{\partial z} - \frac{\partial u}{\partial x} - \frac{\partial v}{\partial y}\right) \\ \tau_{xy} &= \tau_{yx} = \mu\left(\frac{\partial v}{\partial x} + \frac{\partial u}{\partial y}\right) \\ \tau_{xz} &= \tau_{zx} = \mu\left(\frac{\partial u}{\partial z} + \frac{\partial w}{\partial x}\right) \\ \tau_{yz} &= \tau_{zy} = \mu\left(\frac{\partial v}{\partial z} + \frac{\partial w}{\partial y}\right) \\ b_x &= u\tau_{xx} + v\tau_{xy} + w\tau_{xz} + k\frac{\partial T}{\partial x} \\ b_y &= u\tau_{yx} + v\tau_{yy} + w\tau_{yz} + k\frac{\partial T}{\partial y} \\ b_z &= u\tau_{zx} + v\tau_{zy} + w\tau_{zz} + k\frac{\partial T}{\partial z} \end{aligned} \qquad (4)$$

In the equations given above ξ_x, ξ_y, ξ_z, ξ_t, η_x, η_y, η_z, η_t, ζ_x, ζ_y, ζ_z, and ζ_t are the metrics of the transformation, and J^{-1} is the Jacobian of the inverse transformation.

Additionally, μ and k are the molecular or laminar coefficients of viscosity and thermal conductivity respectively, γ is the ratio of specific heats, Ma_∞ is the freestream Mach number, and Re_∞ is the freestream Reynolds number based on freestream conditions and the propeller blade tip radius. Stokes' hypothesis was employed in the writing of the shear stress terms in order to relate the first (laminar) and the second coefficients of viscosity.

The above set of unsteady equations can be solved for laminar flow problems but not for turbulent flows ones because of the very small spatial and temporal scales required and the computational resources this entails. In order to obtain meaningful results for turbulent flow problems, a time-averaged form of these equations is solved. The time-averaged equations, called the Reynolds-Averaged Navier-Stokes equations, have the same form as the original ones presented, except that extra terms such as apparent stresses and heat flux terms appear. Closure for this system of equations is achieved by using an

eddy viscosity hypothesis, which assumes that these extra terms can be related to the gradients of mean flow variables. To this end, the laminar viscosity in the original equations is replaced by an effective viscosity defined as

$$\mu_e = \mu_l + \mu_t \tag{5}$$

where μ_e is the effective viscosity, μ_l is the laminar viscosity, and μ_t is the turbulent eddy viscosity. Also, the thermal conductivity is replaced by the following using a constant Prandlt number assumption

$$k_e = \frac{\gamma}{\gamma - 1}\left[\left(\frac{\mu}{Pr}\right)_l + \left(\frac{\mu}{Pr}\right)_t\right] \tag{6}$$

where again l and t denote laminar and turbulent respectively, and Pr is the Prandtl number. The laminar and turbulent Prandtl numbers are taken to be 0.72 and 0.9 respectively in this work. The eddy viscosity is computed using the algebraic, two-layer, eddy-viscosity model of Baldwin and Lomax[2], and once known the effective thermal conductivity can be calculated. The eddy viscosity is computed separately in the blade-to-blade and the spanwise directions, and then the inverse of the square of the normal distance to the wall d is used to compute the overall eddy viscosity, i.e.,

$$\mu_t = \frac{\left(\dfrac{(\mu_t)_\eta}{1/d_\eta^2}\right) + \left(\dfrac{(\mu_t)_\zeta}{1/d_\zeta^2}\right)}{\left(1/d_\eta^2 + 1/d_\zeta^2\right)} \tag{7}$$

With this particular formulation of the governing equations the flow around a steadily rotating propeller with an inflow at zero angles of incidence and yaw can be treated as steady and results in an algorithm that is far more efficient than one that solves for the unsteady flow field in an inertial reference frame.

Solution Procedure

As mentioned earlier the computational domain is discretised into a contiguous set of structured hexahedral cells as part of a C-H grid system and Equation 1 is integrated over each cell in the domain. A cell-centre finite-volume scheme is employed in the solver, with the cell centre values of the conserved variables representing cell average quantities. At the cell faces central differencing is used for the evaluation of the convective fluxes, while the viscous fluxes are easily evaluated once the values of the velocity and temperature derivatives are known at these locations. These derivatives require careful evaluation and are calculated using the method described by Lacor et al[3].

A controlled amount of artificial dissipation is added to the resulting equations in order to prevent odd-even point decoupling associated with a central-difference scheme and the appearance of undesirable oscillations near shock waves and stagnation points. The artificial dissipation model used is basically the one originally introduced by Jameson, Schmidt, and Turkel[4], and consists of blended first and third differences of the conserved variables for each equation. Anisotropic scaling of the dissipation terms is employed to prevent the addition of excessive dissipation in the high-aspect-ratio cells that are necessary when performing viscous flow calculations. Two different scaling models, by Martinelli[5] and Radespiel[6] respectively, are used and have proven satisfactory.

Following the spatial discretisation, a system of ordinary differential equations is obtained. To integrate these equations in time to a steady- state an explicit, multistage, Runge-Kutta, time-stepping scheme is used. A five-stage scheme is chosen with the artificial dissipation terms being evaluated on the first, third, and fifth stages only, and frozen on the second and fourth. This scheme has good high frequency damping properties, which is important if it is to drive the multigrid scheme described below.

To significantly increase the rate of convergence to a steady state, three well-proven convergence acceleration techniques associated with explicit type schemes are employed concurrently: local time-stepping, implicit residual averaging, and multigrid. With local time-stepping each cell in the computational domain is advanced in time using its own time-step that is determined by stability considerations. Implicit residual averaging is used to both extend the stability range and robustness of the basic time-stepping scheme. The residual smoothing is applied in factored form. A Full approximation storage (FAS) multigrid scheme based on the work of Jameson[7] is employed. For the multigrid process, coarser grids are obtained by deleting every other mesh line in each coordinate direction of the next finer grid. The solution and residuals are transferred to the coarser grid and a forcing function constructed so that the coarse grid solution is driven by the residuals collected from the next finer grid. Corrections are transferred between grid levels using trilinear interpolation. The work split between by the various grid levels is achieved using a fixed cycling strategy. Two alternatives are implemented in the solver: a V-cycle and a W-cycle. The robustness of the multigrid scheme is significantly enhanced by the smoothing of the coarse grid corrections before addition to the fine grid solution. This reduces high-frequency oscillations introduced by the trilinear

interpolation. The factored scheme used for the residual averaging, but with constant coefficients is employed here.

The flow around a propeller with the inflow at zero angles of incidence and yaw is periodic in the circumferential direction from one inter-blade region to the next. It is therefore necessary to solve for the flow in one inter-blade region only. A C-H type mesh is used to discretise the computational domain, with the C-part in the axial direction and the H-part in the circumferential direction. The boundary conditions are implemented using an extra layer of ghost cells exterior to the flow domain and are described in detail by Boyle[8,9].

A Full Multigrid Method (FMG) is used to provide a well-conditioned starting solution for the finest mesh. With the FMG strategy, the solution is initialised on the coarsest of a specified series of grids and iterated for a set number of multigrid cycles using the FAS multigrid scheme. The solution is then transferred to the next finer grid using trilinear interpolation. This process is repeated until the finest mesh level is reached. In the present scheme three FMG levels are typically used and the maximum possible number of multigrid levels used on all grid levels. 50 multigrid cycles are typically performed on each of the coarser grid levels. The freestream values of the variables are used as the starting solution on the coarsest grid.

RESULTS

Case 1: Inviscid Transonic Flow Around the NACA 10-(3)(066)-033 Propeller

The two-bladed NACA 10-(3)(066)-033 propeller[10], shown in Figure 1, is composed of NACA 16 series airfoil sections and has a rectangular planform. A freestream Mach number and an advance ratio of 0.56 and 0.23 were chosen respectively. The blade angle at 75% radius was 45˚. A medium density grid, shown in Figure 2, with 129x49x73 points in the axial, radial, and circumferential directions respectively was used. The results of the test case are presented in Figures 3 to 7. The convergence history is shown in Figure 3. Convergence was rapid with engineering accuracy (i.e., four orders reduction in the residual of the continuity equation) achieved in 105 multigrid cycles and machine zero (i.e., twelve orders reduction) in 492 cycles on the finest grid level. A comparison of computed and measured surface pressure coefficient at two radial locations is shown in Figures 4 and 5. The comparison between the predictions and measurements is very good considering the complexity of the flow field. Note that computed pressures were obtained at the experimental locations using simple interpolation and that the undeformed blade shape, also called the "cold blade" shape, was used for all propeller calculations reported here. Contours of relative Mach number at the cell centres adjacent to the blade pressure and suction surfaces are shown in Figures 6 and 7 respectively. The supersonic flow region and the shock wave on the suction surface can be clearly identified in the figures.

Case 2: Inviscid Transonic Flow Around the SR3 Advanced Propeller

The Hamilton Standard single-rotation propeller, better known as the SR3, is an eight-bladed advanced propeller and is shown in Figure 8. It was designed for a cruise Mach number of 0.8 and incorporated a 45˚ blade sweep angle for both aerodynamic and acoustic purposes. For this test case a 129x33x33 grid was employed. The freestream Mach number was 0.8, the advance ratio was 3.06, and the blade angle at 75% radius was 60˚. A close-up view of the grid on the hub and blade surfaces in shown in Figure 9. Results from this test case are shown in Figures 10 to 14. Once again convergence, shown in Figure 10, is rapid with engineering accuracy and machine zero obtained in 140 cycles and 606 cycles respectively. Computed surface pressure profiles are shown in Figures 11 and 12 and show a smooth variation over the complete chord. Contours of relative Mach number for the pressure and suction surfaces are shown in Figures 13 and 14 respectively and demonstrate the complexity of the flow field

Case 3: Laminar Flow Over a Smooth Flat Plate

The first set of viscous results is for the case of incompressible laminar flow over a smooth flat plate with zero freestream pressure gradient. In order to approximate incompressible flow the freestream Mach number was set at 0.3. The Reynolds number based on plate length was Re_L=1,000,000. This high value was employed to ensure that the calculated boundary layer thickness was small in comparison to the length of the computational domain in the direction normal to the plate. The computational domain had non-dimensional lengths of 1.0, 0.1, and 0.1 in the axial, vertical, and transverse directions respectively. The grid dimensions were 97x97x9 in the axial, vertical, and transverse directions also. Note that only 9 cells were required in the transverse direction as there should be no tranverse variations of the flow variables. The variation of the skin friction coefficient with axial location is shown in Figure 15, while axial and vertical velocity profiles at various axial locations along the plate are presented in Figures 16 and 17 respectively. In the figures the predictions are compared with the exact solutions of Blasius[11]. The axial and vertical velocity profiles compare very well with the Blasius curve. Overall the comparisons are very good.

Case 4: Turbulent Flow Over a Smooth Flat Plate

The second viscous flow test case was for incompressible turbulent flow over a smooth flat plate, also with zero freestream pressure gradient. A computational domain with the same dimensions and

grid density as employed for the previous test case were used for this case also, but with higher grid spacing the vertical direction in order to accurately resolve the laminar wall-layer region. The chosen Reynolds number was Re_L=10,000,000. The results are presented in Figure 18 to 20. Figure 18 shows the calculated and theoretical variation of skin friction coefficient with axial position The two curves differ slightly but show the same variation with axial position. Similar trends in skin friction were also observed by other researchers[12]. Axial velocity profiles at several axial locations are shown in Figure 19. The laminar wall layer, the overlap layer, and the turbulent outer layer are all distinctly captured in each profile. The theoretical law of the wall and logarithmic-overlap layer law are also plotted and compare very well with the predictions. Velocity vectors in the boundary layer near the plate trailing edge are presented in Figure 20.

Case 5: Viscous Transonic Flow Around the NACA 10-(3)(066)-033 Propeller

Preliminary results are presented for the viscous flow around the NACA 10-(3)(066)-033 propeller. Note, however, that the hub profile differs from the one employed for the inviscid flow calculation (see Figure 21). As for the corresponding inviscid flow test case, a freestream Mach number, advance ratio, and blade angle of 0.56, 0.23, and 45˚ were chosen respectively. A grid with a density of 129x49x65 points was employed. Figure 22 shows a close-up view of the grid on the hub and blade surfaces. The grid is clustered near the hub and blade surfaces and near the blade leading and trailing edges. For this test case the boundary layer was assumed to be fully turbulent on the blade surfaces while a location for boundary-layer transition was specified for the hub surface. Contours of relative Mach number at four radial locations are shown in Figures 23 to 26. The radial location increases in each figure and corresponds to a location near the blade root in the first. In each figure a trailing edge wake is clearly visible, but for the most part the boundary layer is attached to the blade surface. A region of boundary layer separation does however occur on the suction surface near the blade trailing edge. Overall the quality of the results is very encouraging.

CONCLUDING REMARKS

A solver has been developed to predict the viscous flow around general propeller geometries under zero angle of incidence and zero angle of yaw inflow conditions. Results from test cases completed have demonstrated the ability of the solver to accurately and efficiently predict inviscid transonic propeller flow fields, and the ability to accurately capture laminar and turbulent boundary layer behaviour. Preliminary results from a viscous transonic propeller flow field calculation are very encouraging.

ACKNOWLEDGEMENTS

This work was partially funded by the Dublin Institute of Technology under the Seed Research Funding Programme and is the result of three years of effort. The author would like to thank the School of Engineering for supporting this research and also Prof. Eli Turkel for his help and advice.

REFERENCES

[1] Holmes, D. G., and Tong, S. S., "*A Three-Dimensional Euler Solver for Turbomachinery Blade Rows*", Journal of Engineering for Gas Turbines and Power, Vol. 107, pp. 258-264, 1985.

[2] Baldwin, B. S., and Lomax, H., "*Thin Layer Approximation and Algebraic Model for Separated Flows*", AIAA Paper No. 78-257, 1978.

[3] Lacor, C., Hirsch, C., Leonard, B., and Lessani, B.*, "A 3D Navier-Stokes Solver Using Unstructured, Hexahedral Meshes With Adaption"*, AIAA Paper No. 99-3364, 1999.

[4] Jameson, A., Schmidt, W., and Turkel, E., "*Numerical Solutions of the Euler Equations by Finite Volume Methods Using Runge-Kutta Time-Stepping Schemes*", AIAA Paper No. 81-1259, 1981.

[5] Martinelli, L., "*Calculation of Viscous Flows Using a Multigrid Method*", Ph.D. Thesis, Department of Mechanical and Aerospace Engineering, Princeton University, Princeton, New Jersey, USA, 1987.

[6] Radespiel, R., Rossow, C., and Swanson, R. C., *"Efficient Cell-Vertex Multigrid Scheme for Three-Dimensional Navier-Stokes Equations"*, AIAA Journal, Vol. 28, No. 8, pp. 1464-1472, 1990.

[7] Jameson, A., *"Multigrid Algorithms for Compressible Flow Calculations"*, MAE Report 1743, Princeton University, Princeton, New Jersey, USA, Text of lecture given at the 2nd European Conference on Multigrid Methods, Cologne, Germany, 1985.

[8] Boyle, F. J., "*Development of CFD Algorithms for Transient and Steady Aerodynamics*", Ph.D. Thesis, Department of Mechanical Engineering, National University of Ireland, Galway, Ireland, 1999.

[9] Boyle, F. J., O'Flaherty, M. P., and Eaton, J. A., "*Three-Dimensional Euler Solutions for Axisymmetric and Non-Axisymmetric Advanced Propeller Flows*", AIAA Paper No. 99-2386, 1999.

[10] Maynard, J. D., and Murphy, M. P., "Pressure Distributions on the Blade Sections of the NACA 10-(3)(066)-033 Propeller Under Operating Conditions", NACA Research Memorandum L9L12, 1950.

[11] White, F. M, Fluid Mechanics, McGraw-Hill Book Company, 4th Edition, 1999.

[12] Liu, F., and Jameson, A., *"Multigrid Navier-Stokes Calculations for Three-Dimensional Cascades"*, AIAA Journal, Vol. 31, No. 10, 1993.

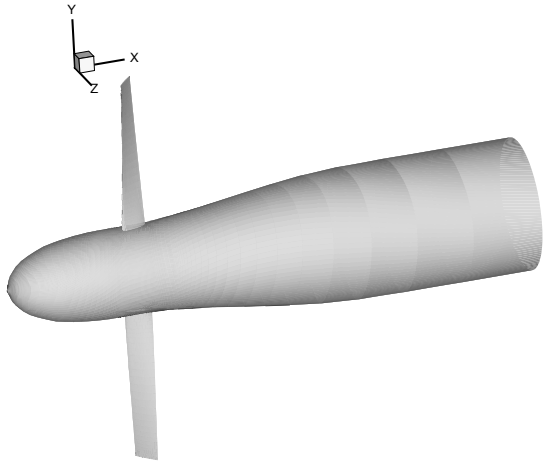

Figure 1. The two-bladed, 10-ft diameter, NACA 10-(3)(066)-033 propeller.

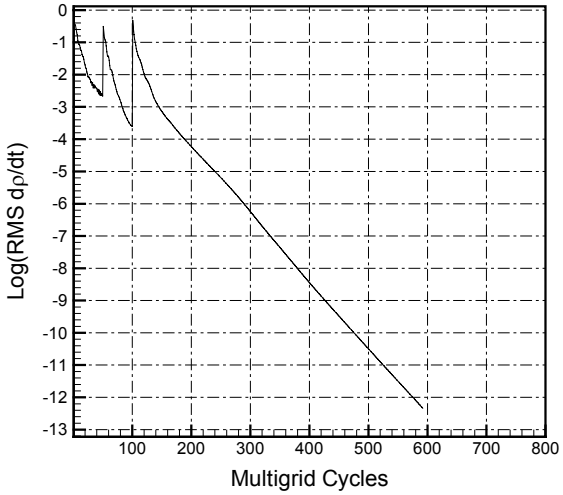

Figure 3. Convergence history of the NACA 10-(3)(066)-033 propeller inviscid flow field calculation. Ma_∞=0.56, J=2.3, and $\beta_{3/4}$=45˚.

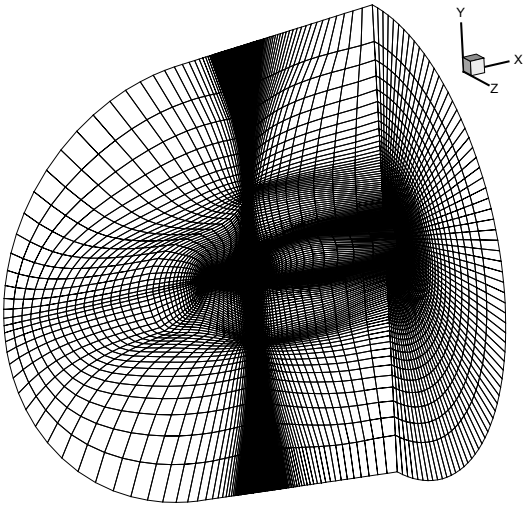

Figure 2. The computational domain and grid for the NACA 10-(3)(066)-033 propeller inviscid flow field calculation.

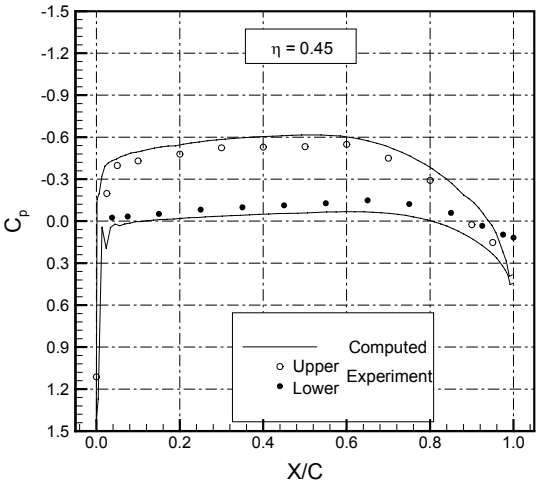

Figure 4. Comparison of chordwise variation of computed and measured surface pressure for the NACA 10-(3)(066)-033 propeller at a radial location of 0.45. Ma_∞=0.56, J=2.3, and $\beta_{3/4}$=45˚.

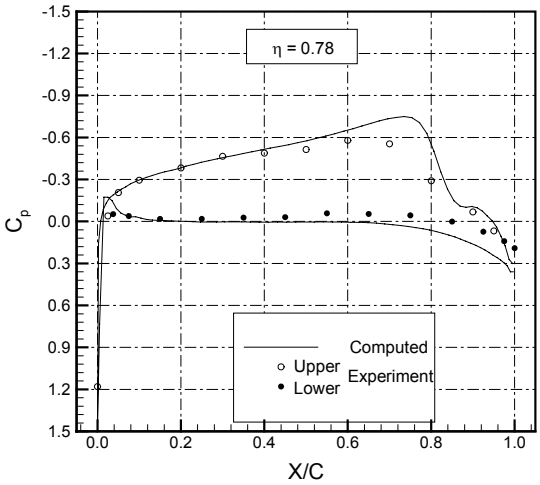

Figure 5. Comparison of chordwise variation of computed and measured surface pressure for the NACA 10-(3)(066)-033 propeller at a radial location of 0.78. Ma_∞=0.56, J=2.3, and $\beta_{3/4}$=45˚.

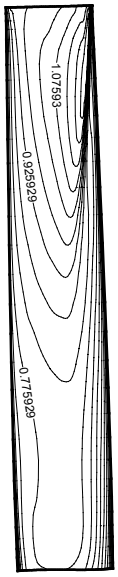

Figure 7. Contours of relative Mach number at the cell centres adjacent to the suction surface of the NACA 10-(3)(066)-033 propeller blade. Ma_∞=0.56, J=2.3, $\beta_{3/4}$=45˚, and ΔMa_{rel}=0.05.

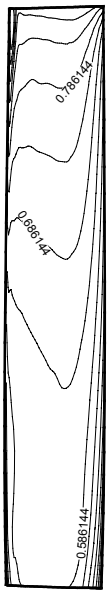

Figure 6. Contours of relative Mach number at the cell centres adjacent to the pressure surface of the NACA 10-(3)(066)-033 propeller blade. Ma_∞=0.56, J=2.3, $\beta_{3/4}$=45˚, and ΔMa_{rel}=0.05.

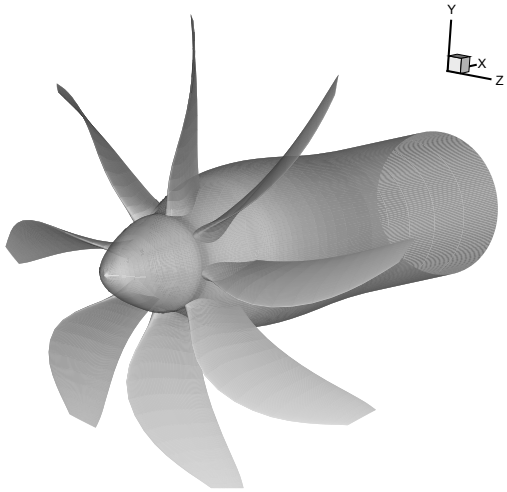

Figure 8. The eight-bladed, advanced SR3 propeller.

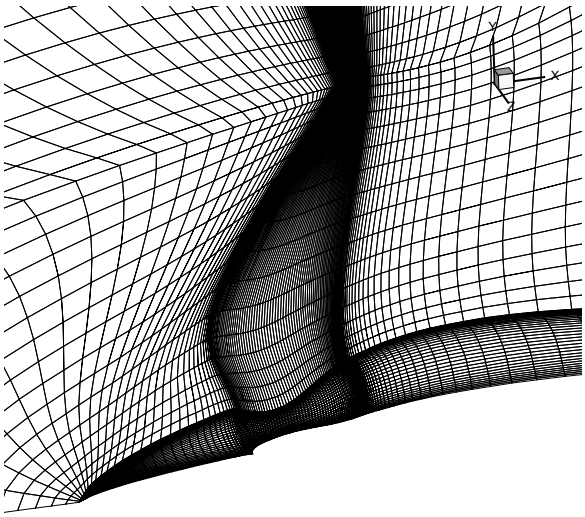

Figure 9. A close-up view of the grid on the hub and blade surfaces of the SR3 propeller.

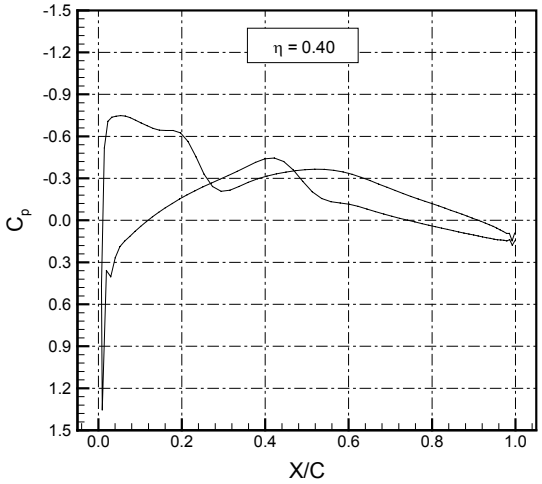

Figure 11. Comparison of chordwise variation of computed and measured surface pressure for the SR3 propeller at a radial location of 0.40. Ma_∞=0.80, J=3.06, and $\beta_{3/4}$=60˚.

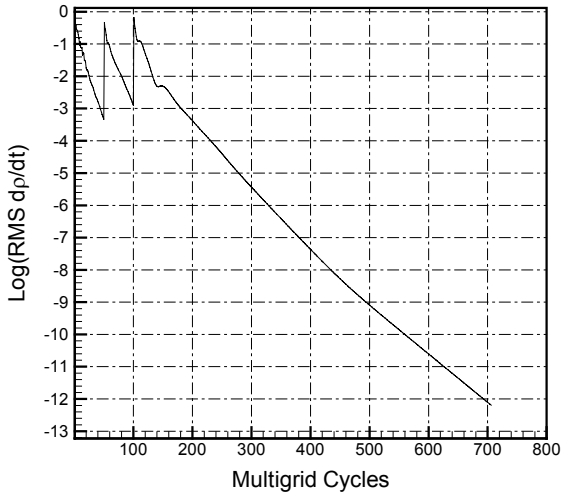

Figure 10. Convergence history of the SR3 propeller inviscid flow field calculation. Ma_∞=0.80, J=3.06, and $\beta_{3/4}$=60˚.

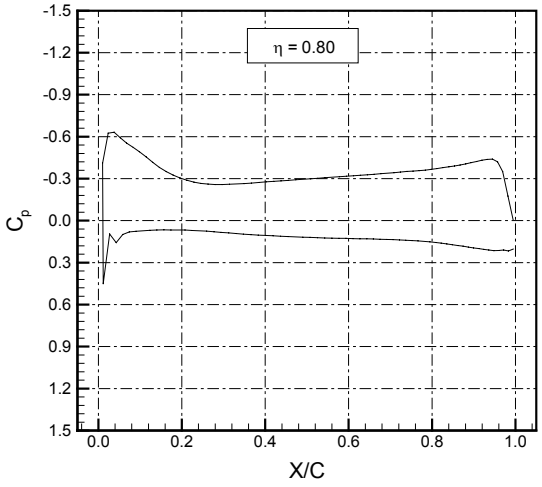

Figure 12. Comparison of chordwise variation of computed and measured surface pressure for the SR3 propeller at a radial location of 0.80. Ma_∞=0.80, J=3.06, and $\beta_{3/4}$=60˚.

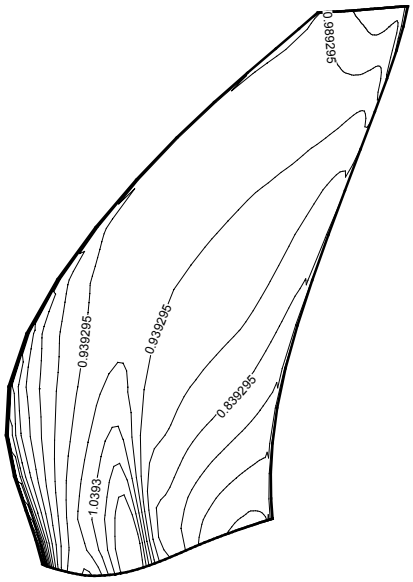

Figure 13. Contours of relative Mach number at the cell centres adjacent to the pressure surface of the SR3 propeller blade. Ma_∞=0.80, J=3.06, $\beta_{3/4}$=60˚, and ΔMa_{rel}=0.05.

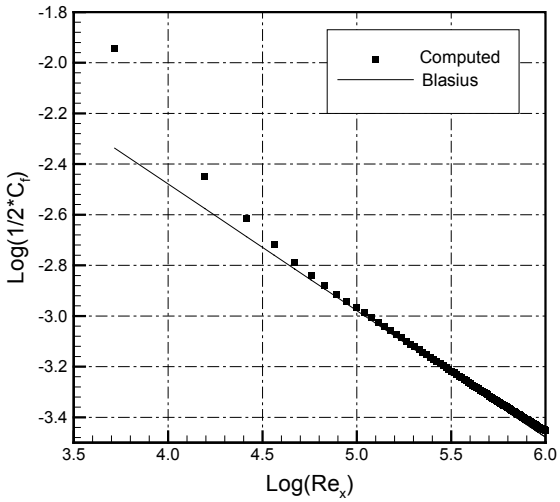

Figure 15. Comparison of predicted skin friction coefficient with Blasius theoretical solution for laminar flow over a flat plate.

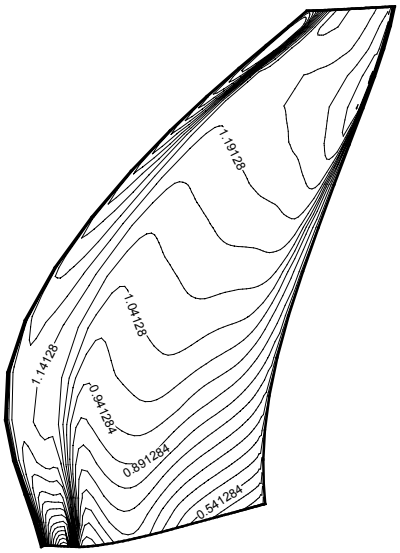

Figure 14. Contours of relative Mach number at the cell centres adjacent to the suction surface of the SR3 propeller blade. Ma_∞=0.80, J=3.06, $\beta_{3/4}$=60˚, and ΔMa_{rel}=0.05.

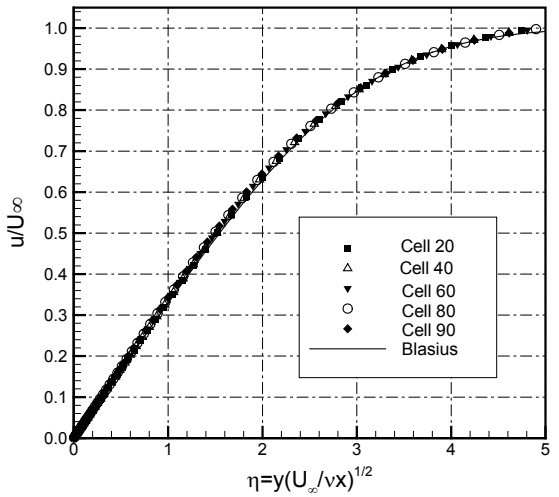

Figure 16. Comparison of predicted axial velocity profiles with Blasius theoretical profile for laminar flow over a flat plate.

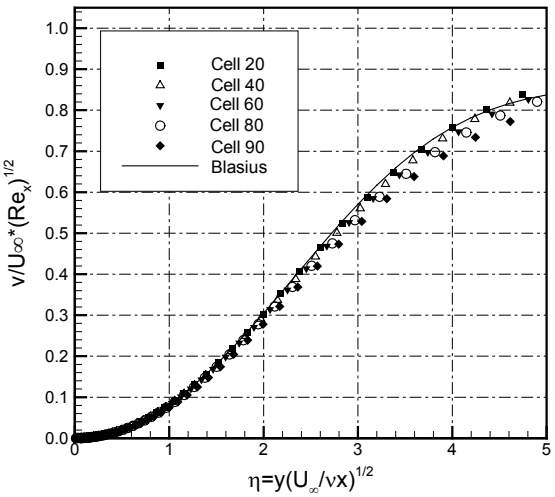

Figure 17. Comparison of predicted vertical velocity profiles with Blasius theoretical profile for laminar flow over a flat plate.

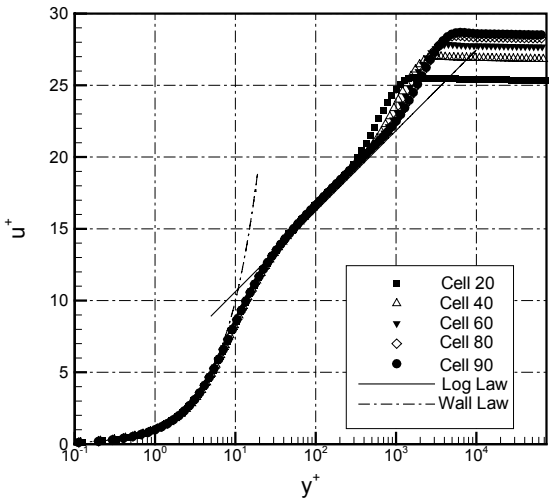

Figure 19. Comparison of predicted axial velocity profiles with theoretical laws for turbulent flow over a flat plate.

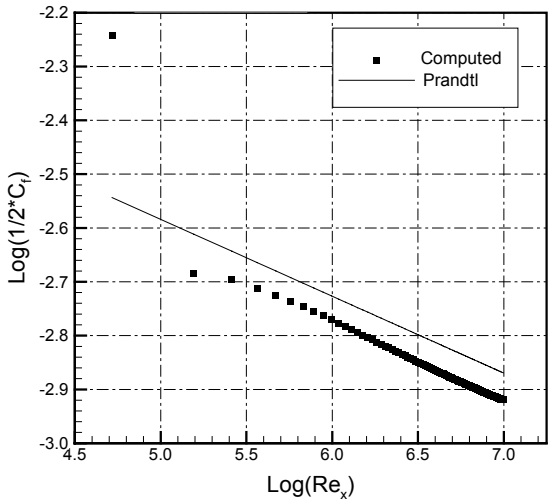

Figure 18. Comparison of predicted skin friction coefficient with Prandtl theoretical solution for turbulent flow over a flat plate.

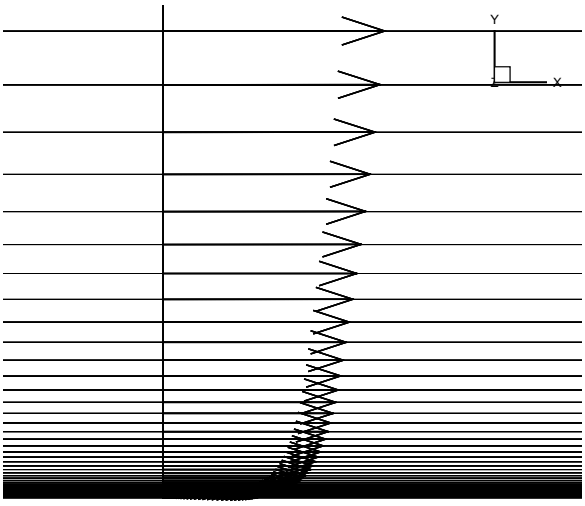

Figure 20. Axial velocity vectors in the turbulent boundary layer at an axial location near the plate trailing edge.

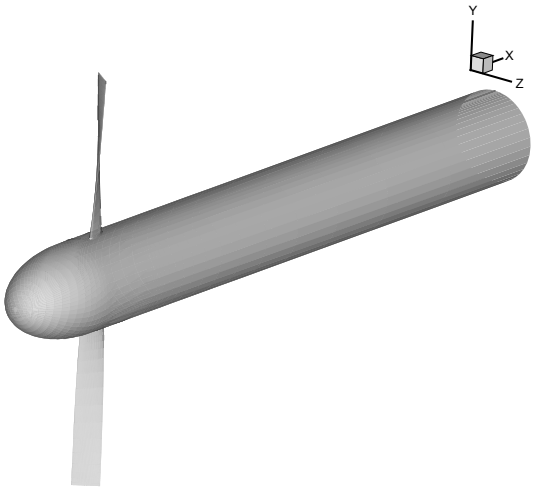

Figure 21. The NACA 10-(3)(066)-033 propeller geometry used for the viscous flow calculation.

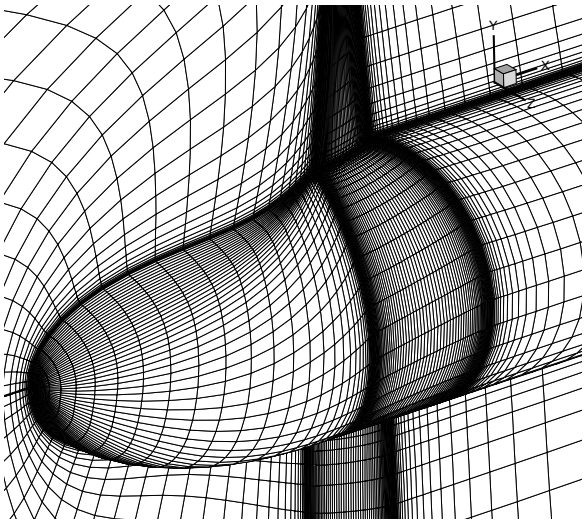

Figure 22. A close-up view of the inner part of the grid around the NACA 10-(3)(066)-033 propeller.

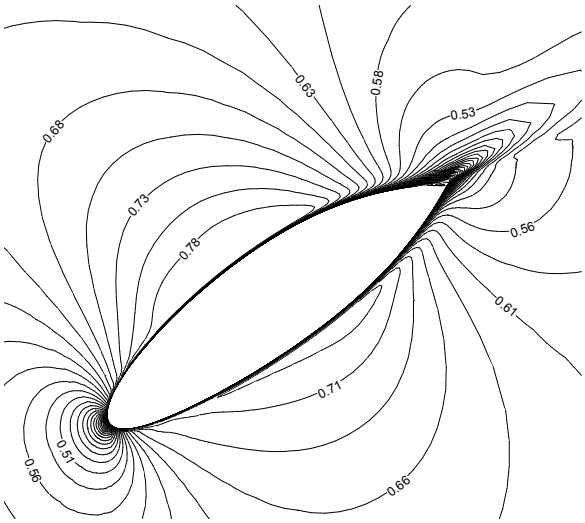

Figure 23. Contours of relative Mach number for the NACA 10-(3)(066)-033 propeller. ΔMa_{rel}=0.025.

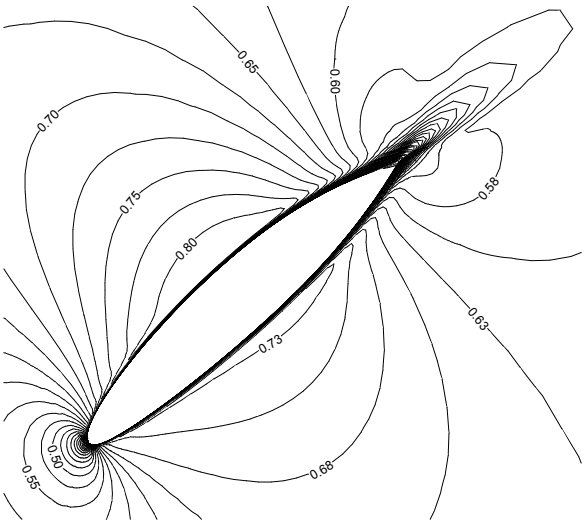

Figure 24. Contours of relative Mach number for the NACA 10-(3)(066)-033 propeller. ΔMa_{rel}=0.025.

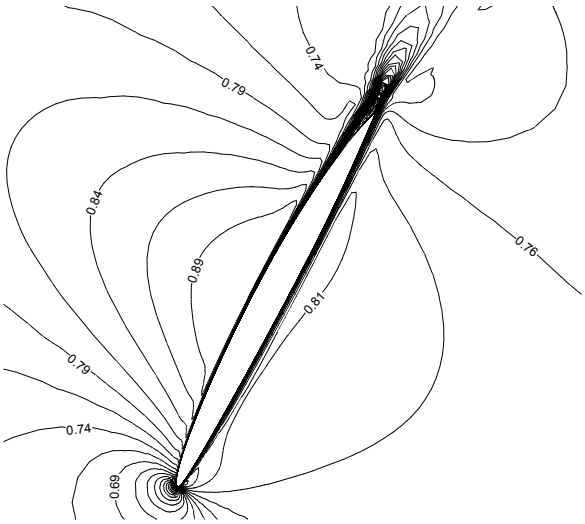

Figure 25. Contours of relative Mach number for the NACA 10-(3)(066)-033 propeller. ΔMa_{rel}=0.025.

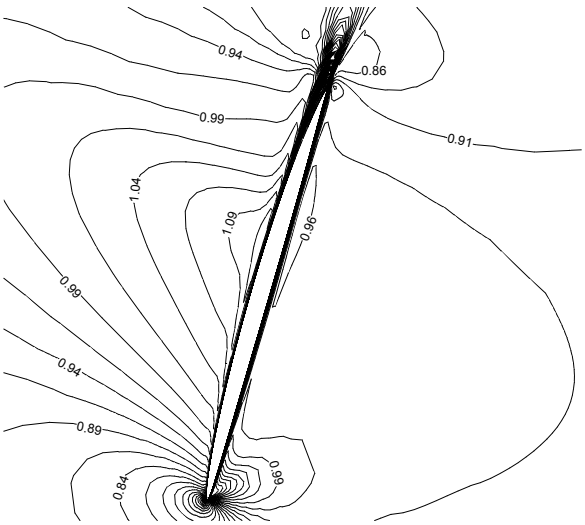

Figure 26. Contours of relative Mach number for the NACA 10-(3)(066)-033 propeller. ΔMa_{rel}=0.025.